SANDIA REPORT

SAND97-0914 • UC-903
Unlimited Release
Printed April 1997

Electromagnetic Imaging of a Fuel Oil Spill at Sandia/CA

L. C. Bartel

Prepared by
Sandia National Laboratories
Albuquerque, New Mexico 87185 and Livermore, California 94550

Sandia is a multiprogram laboratory operated by Sandia Corporation,
a Lockheed Martin Company, for the United States Department of Energy under Contract DE-AC04-94AL85000.

Sandia National Laboratories

Issued by Sandia National Laboratories, operated for the United States Department of Energy by Sandia Corporation.

Available to DOE and DOE contractors from
Office of Scientific and Technical Information
P.O. Box 62
Oak Ridge, TN 37831

Prices available from (615) 576-8401, FTS 626-8401

Available to the public from
National Technical Information Service
U.S. Department of Commerce
5285 Port Royal Rd
Springfield, VA 22161

NTIS price codes
Printed copy: A03
Microfiche copy: A01

SAND97-0914
Unlimited Release
Printed April 1997

Distribution
Category UC-903

Electromagnetic Imaging of a Fuel Oil Spill at Sandia/CA

L. C. Bartel
Geophysical Technology Department
Sandia National Laboratories
P. O. Box 5800
Albuquerque, NM 87185-0705

ABSTRACT

The multifrequency, multisource integral wave migration method commonly used in the analysis of seismic data is extended to electromagnetic (EM) data within the audio frequency range. The method is applied to the secondary magnetic fields produced by a borehole, vertical electric source (VES). The integral wave-migration method is a numerical reconstruction procedure utilizing Green's theorem where the fields are migrated (extrapolated) from the measuring aperture into the interior of the earth. To form the image, the approach used here is to Fourier transform the constructed image from frequency domain to time domain and set time equal to zero. The image is formed when the in-phase part (real part) is a maximum or the out-of-phase (imaginary part) is a minimum; *i.e.*, the EM wave is phase coherent at its origination. In the application here, the secondary magnetic fields are treated as scattered fields. To determine the conductivity, the measured data migrated to a pixel location are equated to calculated data migrated to the same pixel. The conductivity is determined from solving a Fredholm integral equation of the first kind by solving a system of linear algebraic equations. The multifrequency, multisource integral wave-migration method is applied to calculated model data and to actual field data acquired to map a diesel fuel oil spill. For the application discussed here, a two dimensional resistivity slice is calculated from the solution to the Fredholm integral equation. The resistivity image of the fuel oil agrees with the known location.

ACKNOWLEDGMENTS

The author wishes to thank P. M. Drozda, J. E. Uhl, and R. D. Jacobson (all with Sandia/NM) for the expert technical assistance in the acquisition of the data. Special thanks are also extended to M. Moulton and G. E. Sleefe with Sandia/NM and W. T. Hobson, Sandy Leo, and Don Nissen with Sandia/CA, California for their support. The authors also wish to acknowledgments helpful discussions with M. W. Scott both from Sandia/NM and S. A. Urquhart with Zonge Engineering and Research Organization, Tucson, AZ.

This work was supported by the United States Department of Energy under Contract DE-AC04-94AL85000. Sandia is a multiprogram laboratory operated by Sandia Corporation, a Lockheed Martin Company, for the United States Department of Energy. In particular, the Sandia Laboratory Directed Research and Development (LDRD) office provided funding for this work, case number 3515.140.

CONTENTS

Electromagnetic Imaging of a Fuel Oil Spill at Sandia/CA

INTRODUCTION

The need for non-invasive techniques to characterize shallow subsurface geology at environmental sites is now becoming recognized within the environmental industry. Spreading contamination and generating additional hazardous waste (drill cuttings) are some of the risks that accompany even the most careful drilling and sampling operations. Add to this the cost of drilling the large number of boreholes often required for adequate spatial sampling of complex contamination plume geometry and hydrogeological features, and there is ample motivation for developing technologies capable of high resolution, non-invasive imaging of the shallow subsurface. Geophysical imaging is often cited by environmental industry experts as the technology which offers greatest potential for reducing the cost and risk associated with environmental site cleanup.

For the past two decades Sandia National Laboratories has contributed to geophysical technology development through our involvement in a wide variety of defense, energy, and environmental programs. Our goal is technology commercialization in partnership with private industry. Sandia is now aggressively developing new advanced geophysical imaging technologies for shallow environmental applications, with programs in seismic (Harding, 1993; Elbring, 1991, 1993, 1995), electromagnetic (EM) (Alumbaugh and Newman, 1994, 1995; Bartel and Newman, 1991; Bartel, 1992, 1993, 1994; Bartel, *et al.*, 1995; Newman, 1995), and radar imaging. We believe these emerging geophysical technologies will play a major role in future environmental characterization and monitoring operations. The purpose of this report is to introduce one of Sandia's approaches to EM imaging technology for environmental site characterization. A fuel oil spill (FOS) at Sandia/CA, discussed below, provided an opportunity to test both the EM, discussed here, and crosswell seismic imaging methods, discussed elsewhere (Harding, 1993).

In February 1975 at a Sandia/CA site, the accidental puncture of a shallow underground transfer line to an above-ground fuel storage tank resulted in the spill of 225.2 m^3 (59,500 gallons) of No. 2 diesel fuel into the soil. The transfer line was buried about 1.2 m below the land surface. Some of the diesel fuel infiltrated the soil underlying the spill site; the remainder migrated laterally in a light pole trench adjacent to the spill where it is thought to have migrated vertically and laterally below the trench into the unconsolidated soil column. While some fuel was recovered at the surface, an estimated 162 m^3 (43,000 gallons) of diesel remain in the vadose zone soils at the site. Site characterization and remedial investigation studies beginning in the mid-1980's resulted in some 42 test and monitoring wells being drilled on the approximately 1/2 acre site (DOE, 1989). Most of these wells were drilled to the water table, at a depth of 32.31 m (106 feet).

Borehole samples were analyzed for soil type, contamination level, moisture content, porosity, hydraulic conductivity, sieve size, density, cation exchange capacity, pH, and Atterberg limits (DOE, 1989). The contaminant plume, as mapped from the well data, contains maximum

concentration levels of over 20,000 ppm TPH (total petroleum hydrocarbons), with substantial volumes of soil containing over 10,000 ppm TPH. The highest contamination levels were found in fine-grained soils within a 15.24 m (50 feet) horizontal radius of the spill release point, to depths of about 30.48 m (100 feet) (DOE, 1989).

The FOS site was chosen for a demonstration of Sandia crosswell seismic tomography (Harding, 1993) and EM imaging technologies because of the relatively detailed knowledge of site hydrogeology and contaminant distribution obtained during characterization studies. An EM survey was performed in October, 1992, and a crosswell seismic survey was recorded in February, 1993 (Harding, 1993). Discussion of the acquisition, processing, and interpretation of the EM data from the FOS site is presented below.

This report is divided into two sections. The first section will describe the EM integral wave-migration method with application to model calculations and the second part its application to imaging the FOS at Sandia/CA.

EM IMAGING

Background

For the borehole-to-surface and cross-borehole electromagnetic (EM) method under consideration here, the primary EM field is produced by a grounded, borehole, vertical electric source (VES). The VES for cross-borehole magnetometric resistivity (MMR) measurements has been suggested and used by others (Edwards *et al.*, 1984; Nabighian *et al.*, 1984) where generally the VES is operated at a single frequency. In addition borehole-to-surface measurements (using the VES as a source of the primary EM field while measuring the horizontal magnetic fields at the surface) offers additional data that can be used to map the target of interest. The borehole-to-surface method was used by Bartel and Newman (1991) to an map injected salt water plume. The frequency in the MMR case is low enough such that the out-of-phase (imaginary) component is small. However as was shown by Bartel (1992) and, as will be shown here, there is an advantage to operating over a range of frequencies such that the wave migration and extrapolation method (Bartel, 1992), the holographic method (Bartel, 1993), and the integral wave-migration method (Bartel, 1994), discussed below, can be applied to the analysis of data.

For a borehole VES in the earth operating in the audio frequency range (neglecting displacement currents) with an electrical structure which is axially symmetric about the VES, only a magnetic field (**H**) concentric with the VES is created and this field is completely confined to within the earth. In other words, there is no vertical H field created in the earth or in the air. Furthermore, since $\nabla\times\mathbf{H}=0$ (quasi-static limit) in air, it can easily be shown that no horizontal **H** fields are created in the air. The presence of a geoelectric section which is not axially symmetric about the VES produces secondary **H** fields. The measurable vertical **H** fields in a borehole or on the earth's surface and the measurable horizontal **H** fields on the earth's surface are a result of the secondary **H** fields. The advantage of using the borehole VES is that the non-axially symmetric

geoelectric section produces the desired response and the host response is minimized. Figure 1 illustrates the VES method.

In this report the behavior of EM waves in earth materials will be reviewed (Bartel, 1992). The EM holographic method, based on the work of Wu and Toksoz (1987) was successfully used to image a target using data from model calculations. With this success, the method is used to image a diesel fuel oil spill which occurred at the Sandia/CA site as reported by Bartel (1993). The EM wave-migration method (Bartel, 1992) and the EM holographic method (Bartel, 1993) are equivalent. The conductivity structure cannot be determined from the holographic image since the field magnitude is not maintained. The integral wave-migration (extrapolation) method (Bartel, 1994), and discussed below, produces the magnetic field in the earth from which the conductivity structure can be determined.

EM Waves in Earth Materials

The behavior of EM waves in earth materials was discussed briefly by Bartel (1992). Below is a summary of that discussion. For time dependent solutions of the form $\exp(i\omega t)$ ($\omega = 2\pi f$, f is the frequency, and $i = \sqrt{-1}$), the Helmholtz equation for the $\mathbf{H}$ field in the absence of sources is given by (e. g., Ward and Hohmann, 1987, p. 136)

$$\nabla^2\mathbf{H} + k^2\mathbf{H} = 0\,, \tag{1}$$

where k is the magnitude of the wave vector and is defined in the quasi static limit (displacement currents are ignored) as

$$k = \sqrt{-i\omega\mu\sigma}\,, \tag{2}$$

where $\mu = \mu_r\mu_o$ (μ_r is the relative magnetic permeability and $\mu_o = 4\pi\times10^{-7}$ H/m for the free space magnetic permeability), and σ is the electrical conductivity in S/m.

The wave vector defined by equation (2) is complex. The real part of k (k') gives rise to the propagation term and the imaginary part of k (k'') gives rise to the damping term. The phase velocity, v, is defined from the dispersion relation

$$\omega = vk' = v\mathrm{Re}[k]. \tag{3}$$

Thus the phase velocity and the wave length, λ, in the quasi-static limit are given by

$$v = \sqrt{2\omega/\mu\sigma}, \tag{4}$$

$$\lambda = 2\pi v/\omega = 2\pi/k'\,,$$

respectively, which are both dependent upon $\sqrt{f}$. This frequency dependence of the phase velocity leads to the severe dispersion of EM waves in the quasi-static limit. For a pulsed source, this dispersion leads to a spreading of the pulse as it travels through earth materials. For frequencies in the sub-radar and radar range, the dispersion is not as severe leading to generally reasonably good resolution of targets. Even though the waves in the quasi-static limit are very dispersive, they do propagate with a velocity but are significantly damped as they travel through the earth. As was shown in the wave-migration work (Bartel, 1992), the holographic method (Bartel, 1993), and the integral wave-migration method (Bartel, 1994), even for frequencies in the audio range an image can be formed of a target. As will be shown here for the integral wave-migration method, images can be formed utilizing EM waves in the audio range. Higher frequencies will, of course, increase the resolution but may not propagate the desired distances.

Integral Wave-Migration Method

Introduction

In previous work, the migration of electromagnetic (EM) data has been demonstrated (Sasaki, 1989; Bartel, 1992). That previous work was based on the "exploding reflector" model as used in migration of seismic data (Lowenthal, *et al.*, 1976). The EM holographic method discussed by Bartel (1993) was based on the seismic holographic work of Wu and Toksoz (1987) and is equivalent to prestack migration. Schneider (1978) presented an integral formulation for migration where the problem is posed as a boundary value problem. The scalar seismic data measured over an aperture is migrated (extrapolated) using the scalar form of Green's theorem. The integral approach is similar to classical optical diffraction theory (Goodman, 1968). In this report the integral wave-migration method as applied to EM fields discussed by Bartel (1994) is used. Here the mathematical formulation is expanded over the earlier work of Bartel (1994).

The use of the scalar form of Green's theorem for EM waves has some pitfalls as pointed out by Stratton (1941). The use of the scalar form appears to yield correct results for classical optical diffraction because one is dealing with the intensity which is a scalar quantity (Stratton, 1941). When using the scalar form of Green's theorem for the electric and magnetic field components, the migrated components will satisfy the wave equation; however, the migrated fields will not in general satisfy Maxwell's equations (Stratton, 1941). Stratton (1941) stresses using the vector form of Green's theorem for the electric and magnetic field vectors. However as will be shown below, for a Green's function which vanishes on the surface bounding a source-free region, the vector form and the scalar form yield similar results.

The integral formulation of EM wave-migration developed in this paper will be applied to borehole-to-surface EM data. For the borehole-to-surface EM method used here, the primary EM field is produced by a grounded, borehole, VES.

In this report Green's theorem is used to migrate (extrapolate) fields measured over an aperture. The approach here is similar to classical diffraction theory (Goodman, 1968) and its application to seismic data migration (Schneider, 1978; Esmersoy and Oristaglio, 1988). To

produce an image, the backpropagated field is deconvolved with the incident field at each image point (pixel). The backpropagated, deconvolved field is Fourier transformed to the time domain where the time is set to zero and the image is formed when the imaginary part is a minimum (Claerbout, 1971). The EM wave-migration method discussed here, the more traditional migration method discussed previously (Bartel, 1992), and the EM holographic method (Bartel, 1993) are all equivalent for image formation. The advantage of the method discussed in this paper is that the *phases and the magnitudes of the fields are preserved so that the conductivity structure can be determined.* To determine the conductivity, the measured data migrated to a pixel location are equated to calculated data for a yet to be determined conductivity migrated to the same pixel. The conductivity is determined by solving a Fredholm integral equation of the first kind using a conjugate gradient method.

Vector Formulation of Green's Theorem

Stratton (1941) examined the integration of the EM field equations using the vector form of Green's theorem, which is

$$\int_V dv[\mathbf{Q}\bullet\nabla\times\nabla\times\mathbf{P}-\mathbf{P}\bullet\nabla\times\nabla\times\mathbf{Q}] = \int_S ds[\mathbf{P}\times\nabla\times\mathbf{Q}-\mathbf{Q}\times\nabla\times\mathbf{P}]\bullet\mathbf{n} \qquad (5)$$

where V is a volume bounded by the surface S. In equation (5), let $\mathbf{P} = \mathbf{H}$ ($\mathbf{H}$ is the magnetic field) and $\mathbf{Q} = \mathbf{a}\,G^*$ (G^* is the complex conjugate of the Green's function) where $\mathbf{a}$ is a unit vector in an arbitrary direction. Here the magnetic fields are in the frequency domain with a time dependence as discussed above. After some manipulation for a source free region (half-space), equation (5) becomes

$$\mathbf{H}(\mathbf{x},\omega) = -\int_S ds'\{H(\mathbf{x}',\omega)_n\nabla' G^*(\mathbf{x},\mathbf{x}',\omega) + \mathbf{H}(\mathbf{x}',\omega)\partial_n G^*(\mathbf{x},\mathbf{x}',\omega) - \delta_{n\mathbf{a}}\mathbf{H}(\mathbf{x}',\omega)\bullet\nabla' G^*(\mathbf{x},\mathbf{x}',\omega) - G^*(\mathbf{x},\mathbf{x}',\omega)\partial_n\mathbf{H}(\mathbf{x}',\omega) + G^*(\mathbf{x},\mathbf{x}',\omega)\nabla' H(\mathbf{x}',\omega)_n\} \qquad (6)$$

where the subscript n is the outward normal component and $\delta_{n\mathbf{a}}$ is the Kronecker delta which is zero if the vector $\mathbf{a}$ is not in the normal direction. The Green's function $G^*(\mathbf{x},\mathbf{x}',\omega)$ satisfies the equation

$$\left[\nabla^2 + k_o^2\right]G^*(\mathbf{x},\mathbf{x}',\omega) = -\delta(\mathbf{x}-\mathbf{x}'), \qquad (7)$$

where the wave-vector k_o is given by $k_o = \sqrt{-i\omega\mu\sigma_o}$, in the so-called quasi-static limit. μ is the magnetic permeability and σ_o is the electrical conductivity of the host (background) media.

To parallel the diffraction theory as outlined by Goodman (1968), a Green's function will be chosen that vanishes on the aperture S_a; i.e., $\mathbf{x}'$ on S_a. The aperture is part of the surface S that bounds V. The Green's function is defined as

$$G^*(\mathbf{x},\mathbf{x}',\omega) = G^*(\mathbf{x},\mathbf{x}',\omega)_- - G^*(\mathbf{x},\mathbf{x}',\omega)_+ \tag{8}$$

where

$$G^*(\mathbf{x},\mathbf{x}',\omega)_\pm = (1/4\pi)\exp(ik_o r_\pm)/r_\pm \tag{9}$$

$$r_\pm = \left[(x-x')^2 + (y-y')^2 + (z \pm z')^2\right]^{1/2} .$$

G* vanishes on the surface of the earth and as $r_\pm \to \pm\infty$.

For a Green's function G* which vanishes on the surface bounding the volume, the migrated (or extrapolated) field, $\mathbf{H}^e(\mathbf{x},\omega)$, is given by

$$\mathbf{H}^e(\mathbf{x},\omega) = -\int_S ds \mathbf{H}^s(\mathbf{x}',\omega)\partial_n G^*(\mathbf{x},\mathbf{x}',\omega) , \tag{10}$$

$$G^*(\mathbf{x},\mathbf{x}'\omega) = 0 \text{ for } \mathbf{x}' \text{ on S},$$

$\partial_n$is the outward normal derivative and $\mathbf{H}^s(\mathbf{x}',\omega)$ is the secondary or scattered magnetic field evaluated on S. In equation (10) the surface S includes the surface of the aperture S_a, plus the rest of the surface of the earth plus the surface at infinity. Generally, the aperture S_a does not include the entire surface of the earth. For the migration (extrapolation) of measured magnetic fields, equation (10) becomes

$$\mathbf{H}^e(\mathbf{x},\omega) \cong -\int_{Sa} ds' \mathbf{H}^{meas}(\mathbf{x}',\omega)\partial_n G^*(\mathbf{x},\mathbf{x}',\omega), \tag{11}$$

where $\mathbf{H}^{meas}(\mathbf{x}',\omega)$ are the measured fields on the aperture S_a and the fields and $\partial_n G^*$ vanish at infinity. The approximately equal sign is used because the aperture is limited. It is noteworthy that equations (10) and (11) for each component could have been derived from the scalar formulation of Green's theorem.

Secondary Magnetic Fields

From Hohmann (1987, pp 317-319), the vector potential for the secondary field for a primary EM source located at $\mathbf{x}_t$ is given by

$$\mathbf{A}^s(\mathbf{x}', \mathbf{x}_t, \omega) = \int_{V_s} dv'' \, \mathbf{J}^s(\mathbf{x}'', \mathbf{x}_t, \omega) G_1(\mathbf{x}', \mathbf{x}'', \omega), \tag{12}$$

where the secondary or scattering current, $\mathbf{J}^S$, is given by

$$\mathbf{J}^s(\mathbf{x}, \mathbf{x}_t, \omega) = \left[\sigma(\mathbf{x}) - \sigma_o\right] \mathbf{E}(\mathbf{x}, \mathbf{x}_t, \omega). \tag{13}$$

$\mathbf{E}(\mathbf{x}, \mathbf{x}_t, \omega)$ is the total electric field and is the sum of the primary field and the secondary fields, $\mathbf{E} = \mathbf{E}^P + \mathbf{E}^S$ for a transmitter located at $\mathbf{x}_t$, and G_1 is the appropriate Green's function. The volume V_s is the volume of the anomalous conductivity $\sigma(\mathbf{x})$. Thus $\mathbf{J}^S$ exists only in those regions where $\sigma(\mathbf{x}) \neq \sigma_o$. The first order Born approximation ignores the secondary electric field at this point such that

$$\mathbf{H}^s(\mathbf{x}', \mathbf{x}_t, \omega) \cong -\sigma_0 \int_{Vs} dv'' \, \xi(\mathbf{x}'') \mathbf{E}^p(\mathbf{x}'', \mathbf{x}_t, \omega) \times \nabla' G_1(\mathbf{x}', \mathbf{x}'', \omega), \tag{14}$$

where

$$\xi(\mathbf{x}'') = \left[\sigma(\mathbf{x}'') - \sigma_o\right] / \sigma_o. \tag{15}$$

The volume V_s is the volume where $\sigma(\mathbf{x}'') \neq \sigma_o$. If the conductivity structure is known, then the secondary magnetic fields on the surface of the aperture (surface of the earth in this example) can be calculated from equation (14) within the Born approximation. These calculated secondary fields, $\mathbf{H}^s(\mathbf{x}', \mathbf{x}_t, \omega)$, can be migrated (extrapolated) using equation (11) by replacing the measured field by the calculated field.

Determining the Conductivity Structure

In equation (14) it is assumed that the conductivity structure is known. However, in this report the conductivity structure $\sigma(\mathbf{x}'')$ is to be determined from the measured magnetic fields, $\mathbf{H}^{meas}(\mathbf{x}', \omega)$. To determine $\xi(\mathbf{x}'')$ and hence $\sigma(\mathbf{x}'')$, the extrapolated measured field is equated to the extrapolated calculated field. Using equations (11) and (14)

$$\mathbf{H}^e(\mathbf{x},\mathbf{x}_t,\omega) \cong \sigma_o \int_{Vs} dv''\, \xi(\mathbf{x}'')\Gamma(\mathbf{x},\mathbf{x}'',\mathbf{x}_t,\omega), \tag{16}$$

where

$$\Gamma(\mathbf{x},\mathbf{x}'',\mathbf{x}_t,\omega) = \int_{Sa} ds'\, \mathbf{E}^p(\mathbf{x}'',\mathbf{x}_t,\omega) \times \nabla' G_1(\mathbf{x}',\mathbf{x}'',\omega)\partial_n G^*(\mathbf{x},\mathbf{x}',\omega), \tag{17}$$

and $\mathbf{H}^e(\mathbf{x},\mathbf{x}_t,\omega)$ is calculated from equation (11) using the measured data.

The migrated image, Φ_M, is obtained by an imaging condition similar to that used for migration of seismic data. The imaging condition consists of deconvolving the backpropagated field by the incident field at each image point $\mathbf{x}$ and evaluating the resulting function at time zero (Claerbout, 1971; Esmersoy and Oristaglio, 1988). This deconvolution takes into account the phase change of the primary fields between the source and the image point $\mathbf{x}$. Following Esmersoy and Oristagilo (1988) for a source function $S(\mathbf{x},\mathbf{x}_t,\omega)$

$$\Phi(\mathbf{x},\mathbf{x}_t)_M = \sigma_o \int_{Vs} dv''\, \xi(\mathbf{x}'')\Lambda(\mathbf{x},\mathbf{x}'',\mathbf{x}_t), \tag{18}$$

where

$$\Phi(\mathbf{x},\mathbf{x}_t)_M = (1/2\pi)\int_{-\infty}^{\infty} d\omega \mathbf{H}^e(\mathbf{x},\mathbf{x}_t,\omega)/S(\mathbf{x},\mathbf{x}_t,\omega), \tag{19}$$

and

$$\Lambda(\mathbf{x},\mathbf{x}'',\mathbf{x}_t) = (1/2\pi)\int_{-\infty}^{\infty} d\omega \Gamma(\mathbf{x},\mathbf{x}'',\mathbf{x}_t,\omega)/S(\mathbf{x},\mathbf{x}_t,\omega). \tag{20}$$

Equation (18) is a Fredholm integral equation of the first kind for the unknown ξ. It is obvious that the conductivity structure determined from equation (18) may depend upon the component of $\mathbf{H}$ used in the imaging process. Note that the volume V and hence the surface S exclude the source of the primary EM fields. There will be some error in this approach if G* does not vanish on the surface of the source for the primary EM field.

As pointed out by Esmersoy and Oristaglio (1988), $\Lambda(\mathbf{x},\mathbf{x}'',\mathbf{x}_t)$ is the point-spread function for the migrated image at point $\mathbf{x}$. The migrated image is the true conductivity structure "smoothed" by the function Λ. For multiple sources, equation (18) is summed over all transmitting antennae locations before solving for ξ.

It is noteworthy that this approach is similar to the EM holographic method discussed previously (Bartel, 1993) where plane-wave propagators were used. In the previous work, the holographic method was based on the work of Wu and Toksoz (1987).

Figure 2 schematically illustrates the wave-migration method for a borehole VES and surface magnetic field measurements. The migrated, measured magnetic field is integrated over surface aperture (only one receiver station and one image pixel are shown for clarity) and deconvolved with the source. This deconvolution gives the correct phase to the primary field at the image pixel since the measured data are phase referenced to the transmitter. The image is formed by setting time equal to zero for the deconvolved migrated field and the source of the scattered field is at pixels where the phase is near zero (*i.e.*, imaginary part is near zero). The field calculated for a yet to be determined conductivity is also migrated to the image pixel and deconvolved with the source function and time set equal to zero. Comparing the image of the measured data to the "image" of the calculated data results in an integral equation to solve for the conductivity structure. To compare to the above equations, the image pixel is represented by $\mathbf{x}$, the receiver locations by $\mathbf{x}'$, and the calculated points by $\mathbf{x}''$.

The conductivity structure is determined by solving the integral equation, equation (18). The dicretization of equation (18) results in a system of linear algebraic equations to solve for the conductivity structure. Equation (18) then takes the form

$$\Phi = \Lambda * \xi, \tag{21}$$

*where the * denotes matrix multiplication. The column vector Φ are the extrapolated fields, ξ is* the column vector of the unknown conductivity structure, and Λ is a calculated matrix. It is noteworthy that Λ is generally singular (or nearly singular) such that Λ has no direct inverse. In order to stabilize the solutions, a ridge constant, λ, (Marquardt, 1963, 1970) is subtracted from the diagonal elements of Λ to give

$$\Phi = [\Lambda - \lambda \mathbf{I}] * \xi, \tag{22}$$

or can be implemented as given by (Lawson and Hanson, 1974, p. 190)

$$\begin{bmatrix} \Lambda \\ \lambda \mathbf{I} \end{bmatrix} * \xi = \mathbf{Q} * \xi = \begin{bmatrix} \Phi \\ 0 \end{bmatrix}. \tag{23}$$

Here $\mathbf{I}$ is the identity matrix. The Marquardt (1963, 1970) method is also called ridge regression or damped least squares. Note that in practice, the matrix $\mathbf{Q}$ on the left-hand side of equation (23) is made square by multiplying by the transpose of $\mathbf{Q}$, $\mathbf{Q}^T$, such that equation (23) now becomes

$$\mathbf{Q}^T * \mathbf{Q} * \xi = \mathbf{Q}^T * \Phi \tag{24}$$

or

$$\mathbf{A} * \xi = \mathbf{B} .$$

There are a variety of ways to solve equations (22-24). The method chosen for this work is the conjugate gradient method (e.g., see Press, et al., 1992). However, the algorithm that was implemented is a modified version of that given in the MATLAB® User's Guide p 2-179 (1994). The modifications consist of utilizing the ridge constant, equations (22-24), and restricting the ξ vector on output to values such that resistivity is not negative and is constrained to some maximum value. For the solutions discussed below, the solutions were obtained using the ridge regression as implemented through equation (24).

It is noteworthy that the implementation of the ridge constant λ constrains the solution for ξ to be near zero; i.e., $\sigma \approx \sigma_o$. The larger the ridge constant, the more the solution for the conductivity is forced equal to the background conductivity. The smaller the ridge constant, the more the solution for the conductivity is allowed to deviate from the background value; however, the solution can become unstable for too small a ridge constant. The "proper" value for the ridge constant is that value which yields a small residual error with the solution being physically possible.

Results from Model Calculations

The multifrequency, multisource integral formulation for migration method discussed above is applied to model calculations for the geoelectric model shown in Figure 3. This model was chosen so that a comparison to the wave-migration method and holographic method can be made (Bartel, 1992, 1993, and 1994). The horizontal **H**-fields were calculated on a 10 × 10 m surface grid over the target area using an integral equation method (Newman *et al.*, 1986) for the three VES's shown in the figure. The fields were calculated over the frequency spectrum from 4 Hz to 4096 Hz in binary steps. The **H**-fields provided the input for the field components $\mathbf{H}^{meas}(\mathbf{x}, \mathbf{x}_t, \omega)$.

The phase image $\Phi(\mathbf{x})_{My}$ (for the y-component of **H**) is shown in Figure 4 where a resistivity of 10 $\Omega \bullet$ m was used to calculate the magnitude of the background wave vector k_o. The phase of the y-component of the primary magnetic field was used in the deconvolution in equations (19) and (20). Figure 4 shows a cross-section at x = 0 along the y-axis (see Figure 3 for the location). The zero phase is indicative of the source of scattered field. Six frequencies were used for the image, 128 Hz to 4096 Hz in binary steps. The imaged area is divided into 5×5 m pixels from the 5 m to 55 m deep and from y = -20 to 20 m. The image is formed from data calculated at 25 surface data stations for the three transmitters (75 data points in all). The aperture S_a in this case is taken to be 40×40 m for the 25 surface receiver sites. For visual presentation, the image formed on the 9×11 set of 5×5 m pixels was interpolated onto a set 1×1 m pixels covering the same area. The darker areas show where the phase is >0 degrees and the lighter areas show where the phase is <0 degrees. The cross-section of the target is superimposed on the figure.

From an examination of Figure 4 it is clear that the zero phase line yields a concave upward shape and the target is smeared. This effect is similar to that observed in the vertical seismic profile (VSP) data migrated by Esmersoy and Oristaglio (1988); however, in their case the upgoing traces were tapered at the ends of the receiver array to reduce end effects. No attempt is made to reduce end effects or sharpen the image for the EM data given here. It is noteworthy that the secondary currents producing the scattered y-component of the magnetic field are the x-component perpendicular to the plane of the image, and the z-component which is in the plane and in the vertical direction.

The origin of the scattered magnetic field is that region where the imaginary part of the scattered field is a minimum so that the phase is near zero or 180 deg. Therefore to determine the conductivity, $\Phi(\mathbf{x})_{My}$ was set to zero for pixels where the phase did not fall within a somewhat arbitrary constraint of ±10 degrees. The real part of $\Phi(\mathbf{x})_{My}$ that satisfies the constraint condition is denoted as $\hat{\Phi}(\mathbf{x})_{My}$. It is assumed that $\hat{\Phi}(\mathbf{x})_{My}$ images the target. The surface measured secondary fields are assumed to originate where $\hat{\Phi}(\mathbf{x})_{My}$ is non zero. Figure 5 shows the image for the region of the non zero $\left|\hat{\Phi}(\mathbf{x})_{My}\right|$ where the darkest region is where $\left|\hat{\Phi}(\mathbf{x})_{My}\right|$ is zero and the lightest region is where $\left|\hat{\Phi}(\mathbf{x})_{My}\right|$ has the largest magnitude. As for Figure 4, the data were interpolated onto 1×1 m pixels covering the same area. Superimposed on the figure is the location of the target used in the calculations. Since the phase image shown in Figure 4 is smeared, the image of the source of the measured fields is also smeared. However, note that $\left|\hat{\Phi}(\mathbf{x})_{My}\right|$ has a maximum value at the location of the target.

As stated above, the smearing of the target toward the edges of the image is characteristic of the migration process (Esmersoy and Oristaglio, 1988). The origin of this smearing can be illustrated by visualizing the back propagation of the fields as arcs of constant phase emanating from each measuring point. The imaged source of the measured fields is the locus of the intersection of all these arcs of constant phase. Thus for a limited aperture and number of measurement points, the image is not sharp. Increasing the size of the aperture and the number of measurement points will sharpen the image.

The conductivity and hence the resistivity structure is determined from the solutions to the Fredholm integral equation of the first kind, equation (18), or as implemented through equation (24). Since the matrix Λ_y is nearly singular, the use of a ridge constant is necessary in order to obtain a solution. To effect the solution, the constrained $\hat{\Phi}(\mathbf{x})_{My}$ was used for Φ and only the real part of Λ_y was used for Λ. The integral equation is three dimensional. To make a tractable solution for a PC computer, the three-dimensional volume integral (discrete sum) was approximated utilizing a two-dimensional integral (discrete sum) with the integrand in equation (18) held constant in the third dimension. Therefore the conductivity structure will be two-dimensional slices through the earth approximating the actual conductivity values and will be only

indicative of the actual values. The solutions to equation (24) yield values of ξ where ξ is defined by equation (15). The resistivity (the inverse of the conductivity) is given by

$$\rho(\mathbf{x}) = \rho_o \Big/ \left(1+\xi(\mathbf{x})\right), \tag{23}$$

where ρ_o is the background resistivity.

The residual error depends upon the ridge constant used to solve equation (24). Often times the smallest residual error is not necessarily the best, physical answer. From examination of the conductivity structure as a function of ridge constant, the most reasonable solution with an acceptable residual error is usually obtained by using the smallest ridge constant possible while maintaining the assumed areas that have the background resistivity of ρ_o. In other words, the solution should maintain those areas where $\hat{\Phi}(\mathbf{x})_{My}$ is zero where the resistivity is equal to the background value of ρ_o.

It is obvious from Figure 5 that the image of the target is somewhat smeared; therefore the conductivity will also be smeared.. Figure 6 shows the imaged resistivity structure where the background value of resistivity is 10 $\Omega\bullet$m. Note that the data were interpolated onto 1×1 m pixels covering the same area as the original data for visual enhancement. The lighter shades represent the higher values of resistivity, while the darker shades represent the lower values of resistivity. The actual target location in cross-section is superimposed on the figure. The minimum value of the resistivity at the location of the target is approximately 0.5 $\Omega\bullet$m to be compared to a value of 1 $\Omega\bullet$m used in the model calculations. The minimum value of the resistivity coincides with the target area, but the target is not well defined.

The curved nature of the zero-phase surface is probably inherent to the borehole-to-surface method. For a given receiver-transmitter pair, there is a surface of zero phase leading to an ambiguity for the location of the scatterer since the scatterer could be anywhere on that surface to satisfy the imaging condition. This zero-phase surface is defined by the phase change of the primary field between source and scatterer plus the phase change of the scattered field from the scatterer to the receiver which then equals the measured phase. Summation over all receiver-transmitter pairs reduces the ambiguity somewhat but does not eliminate it with the limited number of transmitters and receivers used here. The resulting zero-phase surface is the intersection of all of the individual zero phase surfaces. The conductivity is determined from the value of the real part (in-phase part) of the migrated field. Since the real part of the migrated field varies on this zero-phase surface, the resistivity determined by solving the integral equation will also vary along on this zero phase surface. There is a focusing of the determined resistivity to image the target.

IMAGING OF THE FUEL OIL SPILL SITE

In the fall of 1992, a VES EM experiment was planned and executed at the Sandia/CA FOS site. Figure 7 shows the layout of surface data stations, the location of the four transmitter wells, and one of the monitor wells. The spill release point is also shown in the figure. The surface data stations are on a 10×10 m grid for a total of 49 surface data stations. For the four transmitter/receiver wells, four VES electrodes were installed on the outside of PVC at a spacing of 9.144 m with the bottom electrode at a depth of 31.85 m. Five of the six possible transmitter configurations in each well were used (the one not used was the one using the total length). Data were taken at the 49 surface data stations for the 20 transmitters. The frequency range used was 16 Hz to 4096 Hz in binary steps.

Application of the Integral Wave-Migration Method

The multifrequency, multisource integral formulation for migration method discussed above is applied to the field data taken at the FOS. The horizontal **H** fields were measured on a 10×10 m surface grid over the target area for the four transmitter wells with five VES's in each well. The **H** fields provided the input for the field components $\mathbf{H}^{meas}(\mathbf{x},\mathbf{x}_t,\omega)$ in equation (11).

The phase image of $\Phi(\mathbf{x})_{My}$ (for the y-component of **H**) is shown in Figure 8 where a resistivity of 40 $\Omega\bullet$m was used to calculate the magnitude of the background wave vector k_0. The phase of the y-component of the primary magnetic field was used in the deconvolution in equations (18) and (19). Here the real part of $\Phi(\mathbf{x})_{My}$ is negative when the imaginary part tends to zero. Shown is a cross-section at x = 35 along the y-axis (see Figure 7). For the phase image six frequencies were used, 128 Hz to 4096 Hz in binary steps. The imaged area was divided into 5×5 m pixels from the 5 m to 55 m deep and from y = 0 to 60 m resulting in a grid pattern 13×11 with 143 total number of pixels. The phase image was formed from data measured at 49 surface data stations for the 20 transmitters (980 data points in all). The aperture S_a in this case is taken to be 60×60 m for the 49 surface receiver sites. For this figure and the following figures, the image on the 13×11 grid was interpolated onto a grid of 60×55 covering the same area for visual enhancement. The darker areas show where the phase is <0 degrees and the lighter areas show where the phase is >0 degrees. The sharp transition from light-to-dark is the transition from +180 degrees to -180 degrees.

The origin of the scattered magnetic field is that region where the imaginary part of the scattered field is a minimum so that the phase is near zero or 180 deg. As was done for the model calculations to determine the conductivity, $\Phi(\mathbf{x})_{My}$ was set to zero for pixels where the phase did not fall within a somewhat arbitrary constraint of ±15 degrees in this case. Again the real part of $\Phi(\mathbf{x})_{My}$ that satisfies the constraint condition is denoted as $\hat{\Phi}(\mathbf{x})_{My}$. Figure 9 shows the image for the region of non zero $\left|\hat{\Phi}(\mathbf{x})_{My}\right|$ where the darkest region is where $\left|\hat{\Phi}(\mathbf{x})_{My}\right|$ is zero and the lightest region is where $\left|\hat{\Phi}(\mathbf{x})_{My}\right|$ has the largest value. Since the phase image shown in Figure 8

is smeared, the image of the source of the measured fields and the interpreted resistivity will also be smeared. However, note that $\left|\hat{\Phi}(\mathbf{x})_{My}\right|$ has a maximum magnitude at the location of the spill release point as noted in the figure.

As for the model calculations, the conductivity and hence the resistivity structure is determined from the solutions to the Fredholm integral equation of the first kind, equation (18). To effect the solution, the constrained $\hat{\Phi}(\mathbf{x})_{My}$ was used for Φ and only the real part of Λ_y was used for Λ. As was done for the model calculations to make a tractable solution for a PC computer, the three-dimensional volume integral (discrete sum) was approximated utilizing a two-dimensional integral (discrete sum) with the integrand in equation (24) held constant in the third dimension. Therefore the conductivity structure will be two-dimensional slices through the earth approximating the actual conductivity structure and will be only indicative of the actual structure.

Figure 10 shows the imaged resistivity structure where the background value of resistivity of 40 $\Omega\bullet$m was used for σ_o and k_o. The lighter shades represent the higher values of resistivity, while the darker shades represent the lower values of resistivity. The spill release point is noted on the figure. For the area under the spill release point, the interpreted resistivity values range from a low value of ~22 $\Omega\bullet$m to a highest value of ~41$\Omega\bullet$m. The region of maximum of $\left|\hat{\Phi}(\mathbf{x})_{My}\right|$ and the minimum values of the resistivity coincide with the spill release point where the highest concentrations of the diesel fuel were measured (approximately 10,000 mg/kg) (DOE, 1989). The spill release point was at a location of approximately 2 m north of the FTA well (x = 33 m, y = 37 m in Figure 7). The end of the light pole trench was approximately 2 m west of the spill release point. It is noteworthy that the resistivity anomalies at the y-location of 20 m are probably associated with the transmitters in the well located near the y = 20 m location (see Figure 7).

Normally one would expect that introduction of fuel oil would lead to an increase in resistivity since the molecular structure of fuel oil is non-polar. The interpretation of the low resistivity region corresponding to directly below the spill release point is that natural bioremediation has taken place leaving behind carbon-type by-products and a decrease in resistivity from the background value. The fact that natural bioremediation takes place almost immediately for fuel oil, gasoline, etc., is known (Mazzella, pers. comm.). The spill occurred in 1975 and these data were taken in 1992 near the end of a long drought period for California. The region of slightly higher than background resistivity below the spill release point at a depth of approximately 35 m may be un-bioremediated fuel oil "floating" on the water. Subsequent to when these data were taken, heavy rains raised the water table sufficiently to enter sampling screens, at which time fuel oil was detected in the water (Hobson, pers. comm.). It is noteworthy that no hydrocarbons were detected when the four transmitter wells were drilled just prior to data acquisition (Hobson, pers. comm.).

For 40 $\Omega\bullet$m earth material, the wave length at 4096 Hz is 312 m. Here as for the model calculations, targets can be detected but the resolution is limited. Again the focusing action of the integral wave-migration method improves the resolution somewhat. It is noteworthy that at a

frequency of 4096 Hz in 40 $\Omega \bullet$ m earth material, there is a 1.15 deg./m phase shift for an EM plane wave traveling through the earth.

SUMMARY AND CONCLUSIONS

The multisource integral wave-migration method described by Schneider (1978) and Esmersoy and Oristaglio (1988) for seismic imaging has been adapted for use on EM data. The integral wave-migration reconstruction of calculated model data are in good agreement with the actual model calculations. The EM integral wave-migration reconstruction was applied to VES EM data taken at a diesel fuel oil spill site. The reconstructed image agrees very well with the location of the spill release point where the majority of the fuel oil remains in the subsurface. For the frequencies used in the reconstructions the targets are detected; however, the resolution of the target is limited by the frequencies involved.

From the work done to date, areas of future research are apparent. The first is the implementation of the method on a larger computer so that the full three-dimensional problem can be addressed. The second is a methodology of combining borehole-to-surface and cross-borehole data to be able to utilize the total data set. On the experimental side, in order to gain resolution it will be necessary to operate at higher frequencies.

REFERENCES

Alumbaugh, D. L. and Newman, G. A., 1994, Fast frequency domain electromagnetic modeling using finite differences: Expanded abstracts 64th Ann. Internat. Mtg. Soc. Explor. Geophys., Los Angeles, CA, Oct. 23-28, 369-373.

Alumbaugh, D. L. and Newman, G. A., 1995, Simulation of airborne electromagnetic measurements in three dimensional environments: Proc. of the Symp. on the Appl. of Geophys. to Engin. and Envir. Problems, Orlando, FL, April 23-26, 319-328.

Bartel, L. C and Newman, G. A., 1991, Mapping a 3-D conductivity anomaly using a vertical electric source - field results: Expanded abstracts 61st Ann. Internat. Mtg. Soc. Explor. Geophys, Houston, TX, Nov. 10-14, 472-475.

Bartel, L. C., 1992, Application of wave migration to borehole vertical electric source EM data: Expanded abstracts 62nd Ann. Internat. Mtg. Soc. Explor., New Orleans, LA, Oct. 25-29, 506-510.

Bartel, L. C., 1993, Application of EM holographic methods to borehole vertical electric source data to map a fuel oil spill. Expanded Abstracts 63rd Ann. Internat. Mtg. Soc. Explor. Geophys, Washington, DC Sept. 26-30, pp. 373-376.

Bartel, L. C., 1994, Integral wave-migration method applied to electromagnetic data: Expanded abstracts 64th Ann. Internat. Mtg. Soc. Explor. Geophys., Los Angeles, CA Oct. 23-28, 361-364.

Bartel, L. C., Wilt, M. J., and Tseng, H-W., 1995, Borehole-to-surface electromagnetic methods: Proc. of the Symp. on the Appl. of Geophys. to Engin. and Envir. Problems, Orlando, FL, April 23-26, 775-783.

Claerbout, J. F., 1971, Toward a unified theory of reflector mapping: Geophysics, **36**, 467-481.

DOE, 1989, Sandia National Laboratories, Livermore, Fuel Oil Spill: U.S. Department of Energy, Albuquerque Operations Office, Environment and Health Division, ER Programs Project Group, April.

Edwards, R. N., Nobes, D. C, and Gomez-Trevino, E., 1984, Offshore electrical exploration of sedimentary basins - The effects of anisotropy in horizontally isotropic layered media: Geophysics, **49**, 556-576.

Elbring, G. J., 1991, Crosshole shear-wave seismic monitoring of an *in situ* air stripping waste remediation process: Sandia National Laboratories Report, SAND91-2742.

Elbring, G. J., 1993, Crosswell seismic imaging of an *in situ* air stripping waste remediation process: Proc. of the Symp. on the Appl. of Geophys. to Engin. and Envir. Problems, San Diego, CA, April 18-22, 55-63.

Elbring, G. J., 1995, Cross borehole seismic tomography at the USDOE Hanford site: Presented at The 1st Symp. on the Hydrogeology of Washington State, The Evergreen State Coll., Olympia, WA, August 28-30.

Esmersoy, C. and Oristaglio, M., 1988, Reverse-time wave-field extrapolation, imaging, and inversion, Geophysics, **53**, 920-931.

Goodman, J. W., 1968, Introduction to Fourier Optics, McGraw-Hill, 34-45.

Harding, R.S., Jr., 1993, Seismic and EM methods for hydrocarbon spill mapping, Computational Technology Initiative for the Oil & Gas Industry Conference, June 20-24, 1993 in Santa Fe, New Mexico.

Hohmann, G. W., 1987, in Electromagnetic Methods in Applied Geophysics - Theory Vol. 1, ed. Nabighian, M. N., Soc. of Exploration Geophysics, 317-319.

Lawson, C. L. and Hanson, R. J., 1974, Solving Least Squares Problems, Prentice-Hall, Inc., 188-194.

Lowenthal, D., Lu, L., Roberson, R., and Sherwood, J. W. C., 1976, The wave equation applied to migration: Geophys. Prosp., **24**, 380-399.

Marquardt, D. W., 1963, An algorithm for least-squares estimation of nonlinear parameters: J. Soc. Indust. Appl. Math., **11**, 431-441.

Marquardt, D. W., 1970, Generalized inverses, ridge regression, biased linear estimation and nonlinear estimation: Technometrics, **12**, 591-612.

MATLAB® High-Performance Numeric Computation and Visualization Software - User's Guide, 1994, The Math Works, Inc., 2-179.

Nabighian, M. N., Opplinger, G. L., Edwards, R. N., Lo, B. B., and Chessman, S. J., 1984, Cross-hole magnetometric resistivity (MMR): Geophysics, **49**, 1313-1326.

Newman, G. A., Hohmann, G. W., and Anderson, W. L., 1986, Transient electromagnetic responses of a three dimensional body in a layered earth: Geophysics, **51**, 1608-1627.

Newman, G. A., 1995, Crosswell electromagnetic inversion using integral and differential equations: Geophysics, **60**, 899-911.

Sasaki, Y., 1989, Application of phase-shift migration to magnetotelluric data: Exp. Abs. 59th Int'l. Ann. Mtg. Soc. Explor. Geophysicists, Dallas, TX, Oct. 29-Nov. 2, 165-167.

Schneider, W. A., 1978, Integral formulation for migration in two and three dimensions, Geophysics, **43**, 49-76.

Stratton, J. A., 1941, Electromagnetic Theory, McGraw-Hill, 460-470.

Ward, S. H. and Hohmann, G. W., 1987, Electromagnetic theory for geophysical applications: in Electromagnetic Methods in Applied Geophysics, **1**, Soc. Explor. Geophys.

Wu, R. S. and Toksoz, M. N., 1987, Diffraction tomography and multisource holograph applied to seismic imaging: Geophysics, **52**, 11-25.

FIGURES

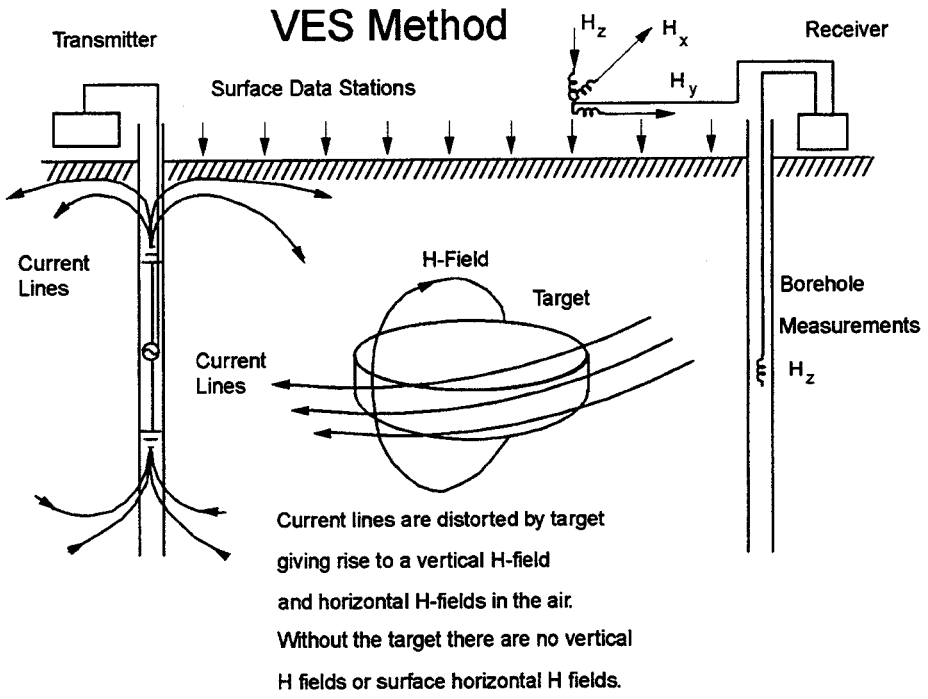

Fig. 1 Schematic illustration of the vertical electric source (VES) method.

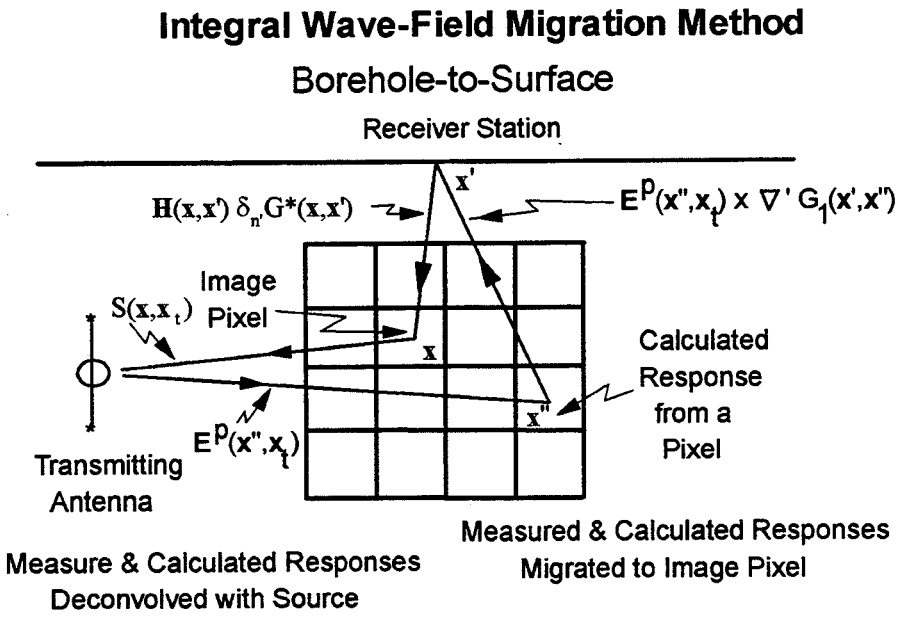

Fig. 2 Illustration of the integral wave migration method. In the figure $\mathbf{x}$, $\mathbf{x}'$, and $\mathbf{x}''$ represent the image, measured data, and calculated field locations, respectively.

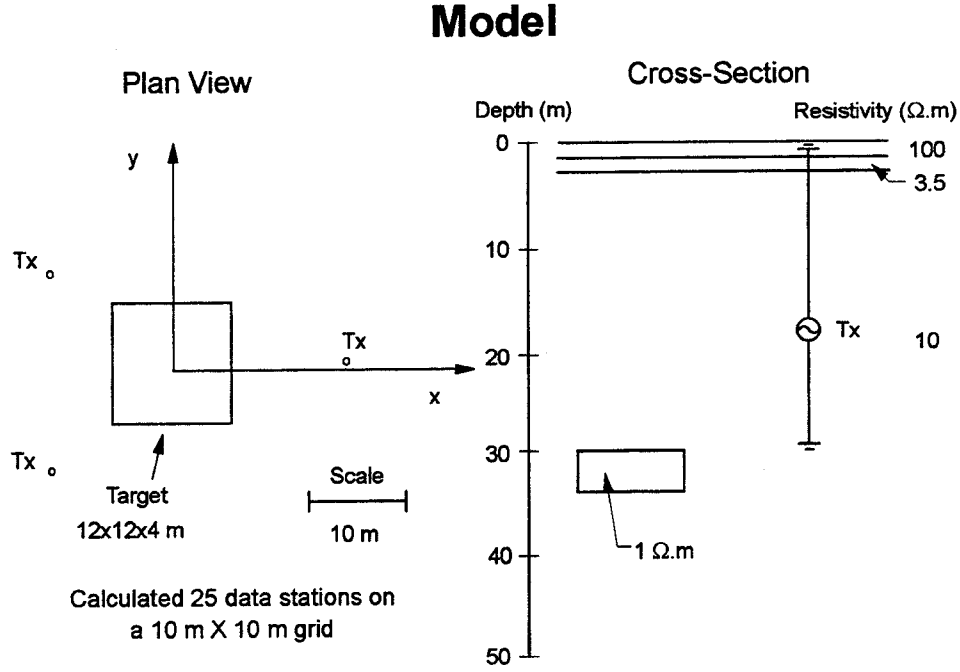

Fig. 3 Plan view and cross-section for model used in calculations. Note only one transmitter is shown for the cross-section view.

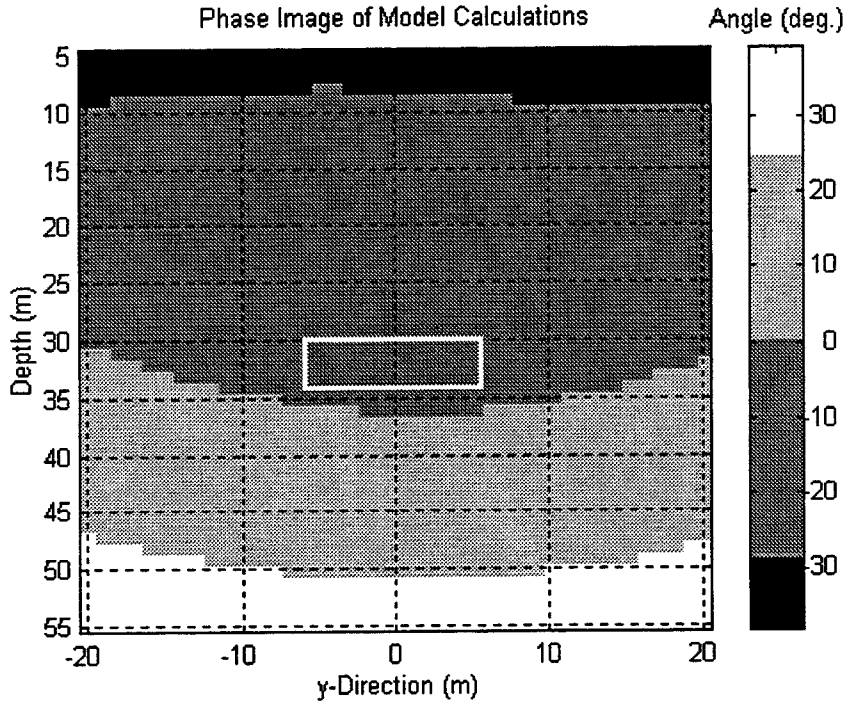

Fig. 4 2-D phase image of model calculation as a function of y and z at x=0. The actual location of the target is superimposed on the figure.

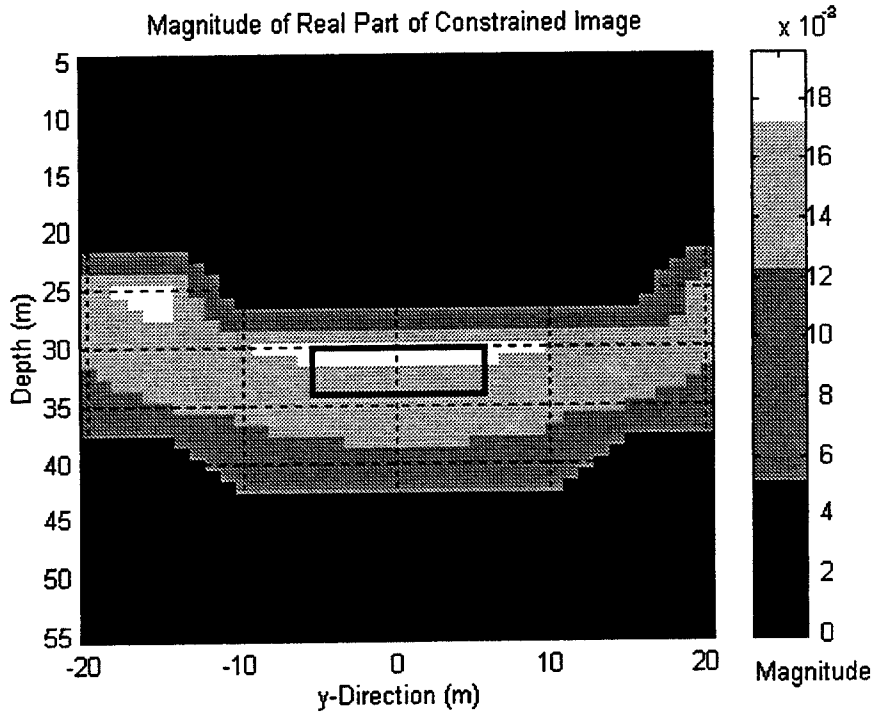

Fig. 5 2-D magnitude of the real part of the constrained image. Phase constraint used was ±10 degrees. The actual location of the target is superimposed on the figure.

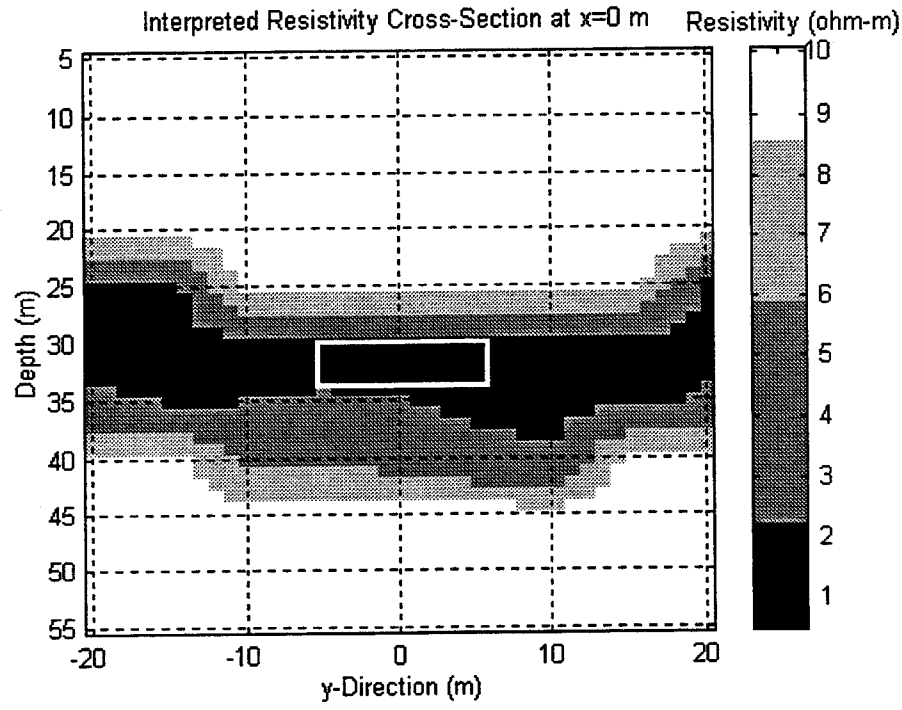

Fig. 6 2-D interpreted resistivity image at x=0 m along the y-direction. The actual location of the target is superimposed on the figure.

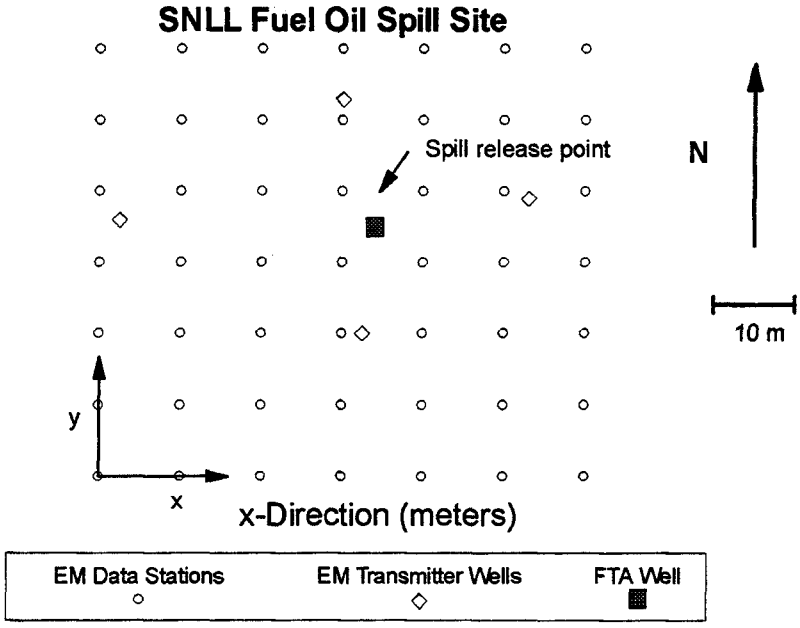

Fig. 7 FOS experimental layout. Surface data stations are on a 10×10 m grid. Shown is the spill release point.

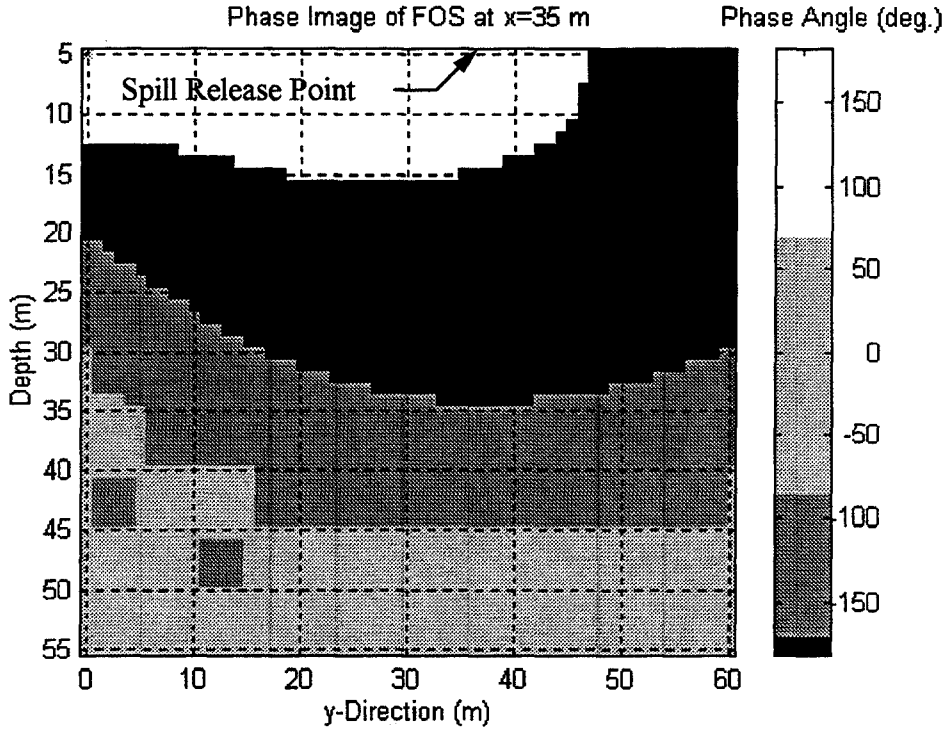

Fig. 8 2-D phase image of the FOS at x=35 m.

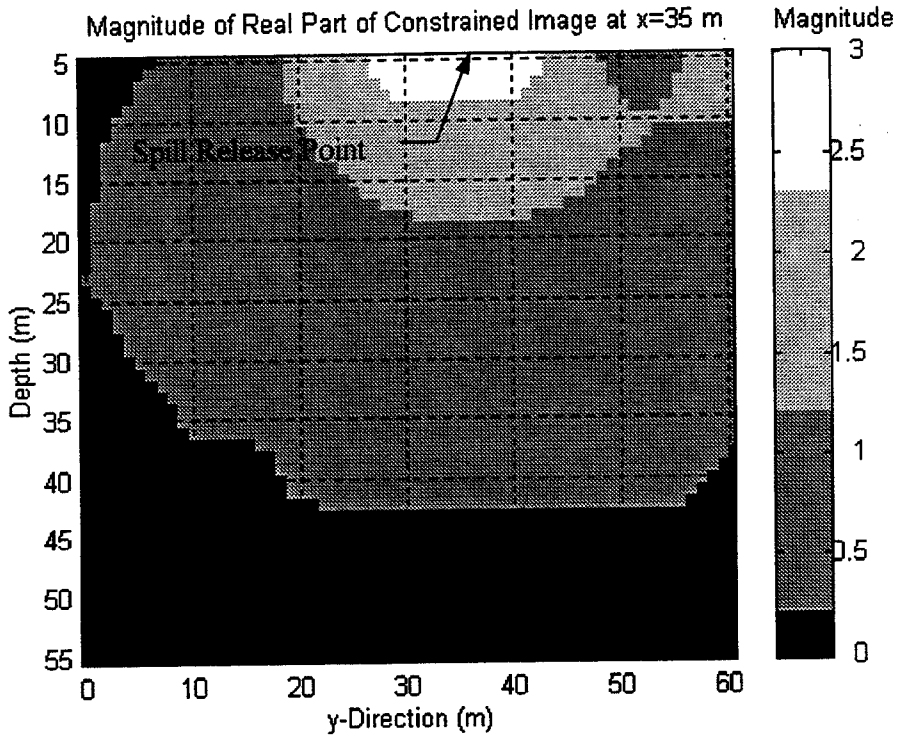

Fig. 9 2-D magnitude of the real part of the constrained image of the FOS at x=35 m. Phase constraint used was ±15 deg.

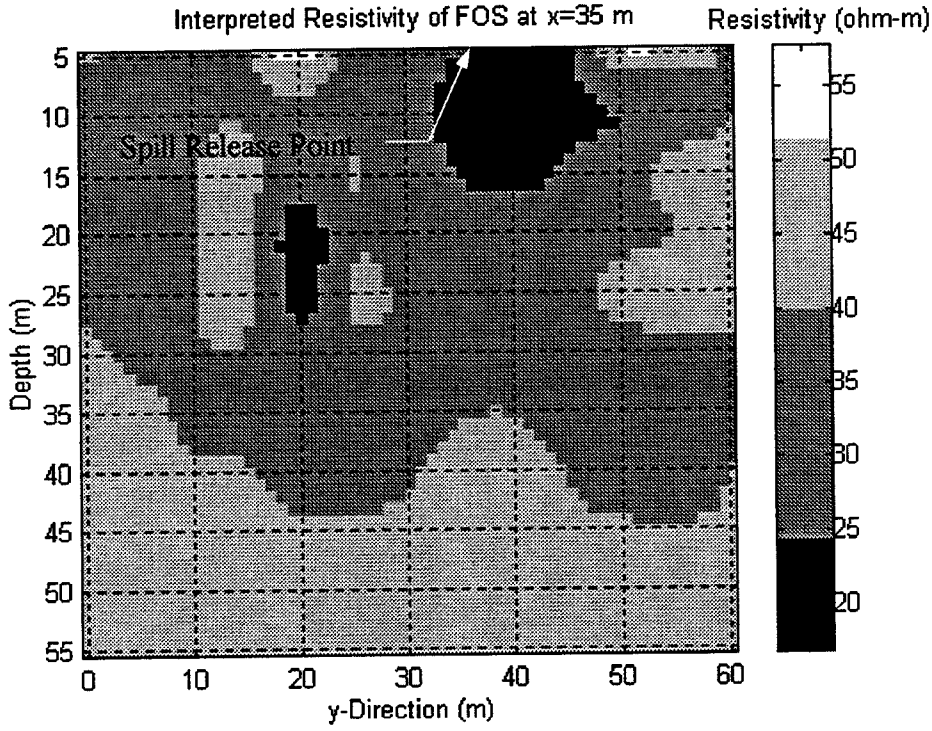

Fig. 10 2-D interpreted resistivity of the FOS at x=35 m.

Distribution:

2 S. A. Urquhart
Zonge Engineering and Research Organization
3322 East Fort Lowell Road
Tucson, AZ 85716

5	0899	Technical Library, 4414
1	0188	C. E. Meyers, 4523
1	0877	D. H. Cress, 5933
1	0573	H. M. Poteet, 5933
1	1033	R. D. Jacobson, 6111
25	0705	L. C. Bartel, 6116
1	0705	T. W. H. Caffey, 6116
1	0705	J. E. Uhl, 6116
1	0750	M. C. Walck,6116
1	0750	D. L. Alumbaugh, 6116
1	0750	D. J. Borns, 6116
1	0705	G. J. Elbring, 6116
1	0750	G. A. Newman, 6116
1	0865	P. M. Drozda, 6116
1	9409	R. P. Nissen, 8250
1	9221	A. T. Leo, 8413
1	9105	W. T. Hobson, 8419
1	9018	Central Technical Files, 8940-2
2	0619	Review and Approval Desk, 12630 For DOE/OSTI
3	0161	Patent and Licensing Office, 11500